

# Precision of diffuse 21-cm lensing

Tingting Lu,<sup>1\*</sup> Ue-Li Pen,<sup>2†</sup>

<sup>1</sup> *Department of Astronomy and Astrophysics, University of Toronto, M5S 3H4, Canada*

<sup>2</sup> *Canadian Institute for Theoretical Astrophysics, University of Toronto, M5S 3H8, Canada*

version 1 October 2007

## ABSTRACT

We study the limits of accuracy for weak lensing maps of dark matter using diffuse 21-cm radiation from the pre-reionization epoch using simulations. We improve on previous “optimal” quadratic lensing estimators by using shear and convergence instead of deflection angles. We find that non-Gaussianity provides a limit to the accuracy of weak lensing reconstruction, even if instrumental noise is reduced to zero. The best reconstruction result is equivalent to Gaussian sources with effective independent cell of side length  $2.0h^{-1}$  Mpc. Using a source full map from  $z=10-20$ , this limiting sensitivity allows mapping of dark matter at a Signal-to-Noise ratio (S/N) greater than 1 out to  $l \lesssim 6000$ , which is better than any other proposed technique for large area weak lensing mapping.

**Key words:** Cosmology-theory-simulation-observation: gravitational lensing, dark age, dark matter, large-scale structure, reionization, non Gaussianity

## 1 INTRODUCTION

The lens mapping of dark matter is an essential cornerstone of modern precision cosmology. Weak gravitational lensing has developed rapidly over the past years, which allows the measurement of the projected dark matter density along arbitrary lines-of-sight using galaxies as sources. Recently, Smith et al. (2007) have demonstrated the first CMB lensing detection. The goal is now to achieve high precision cosmological measurements through lensing, at better than 1% accuracy.

Galaxies are plentiful on the sky, but their intrinsic properties are not understood from first principles, and must be measured from the data. Future surveys may map as many as  $10^{10}$  source objects. Using galaxies as lensing sources has several potential limits (Hirata & Seljak 2004), including the need to calibrate redshift space distributions and PSF corrections, to be better than the desired accuracy, say 1%. This will be challenging for the next generation of experiments.

Some sources, such as the CMB, are in principle very clean, since its redshift and statistical properties are well understood. Unfortunately, there is only one 2-D CMB sky with an exponential damping at  $l \gg 1000$ , which limits the number of source modes to  $\sim 10^6$ .

The potential of detecting the 21-cm background from the dark ages will open a new window for cosmological detections. Studying the 21-cm background as high redshifts lensing source, as well as the physics of the 21-cm background itself, provide rich and valuable information to the evolution of universe. The number of modes on the sky is potentially very large, with numbers of  $10^{16}$  or more. For this reason, 21-cm lensing has recently attracted attention. However, most of the reconstruction methods are based on a Gaussian assumption (Pen 2004; Cooray 2004; Zahn & Zaldarriaga 2006; Benton Metcalf & White 2006; Hilbert et al. 2007). In contrast to CMB lensing, where the Gaussian assumption works well, non-Gaussianity in 21-cm lensing may affect the results. Non-linear gravitational clustering leads to non-Gaussianity, and ultimately to reionization. In this paper, we will address the problem of the lensing of pre-reionization gas.

21-cm emission is similar to CMB: both are diffuse backgrounds. It is natural to apply the techniques used in CMB lensing. Hu & Okamoto (2002) expand the CMB lensing field in terms of the gravitational potential (or deflection angles),

\* E-mail: ttlu@cita.utoronto.ca

† E-mail: pen@cita.utoronto.ca

and construct a trispectrum based quadratic estimator of potential with maximum S/N. However, unlike CMB, the 21-cm background has a 3-D distribution and is intrinsically non-Gaussian. A fully 3-D analysis is explored in Zahn & Zaldarriaga (2006), where they generalize the 2-D quadratic estimator of CMB lensing (Hu & Okamoto 2002) to the 3-D Optimal Quadratic Deflection Estimator (OQDE).

A local estimator was proposed in Pen (2004), which assumed a power law density power spectrum. In this paper, we will design localized estimators for the lensing fields under the Gaussian assumption, and apply the derived reconstruction technique to Gaussian and non-Gaussian sources. The influence of non-Gaussianity can be measured by comparing the numerical results between the Gaussian sources and non-Gaussian sources.

Quadratic lensing reconstruction is a two point function of the lensed brightness temperature field of the 21-cm emission. In the paper, 3-D quadratic estimators are constructed for the convergence ( $\kappa$ ), as well as the shear ( $\gamma$ ). Our method recovers the  $\kappa$  and  $\gamma$  directly instead of gravitational potential or deflection angles. Our estimators have in principle the same form as the OQDE, consisting of the covariance of two filtered temperature maps. The OQDE reconstructs the deflection angle, while our estimators reconstruct the kappa and shear fields. Our filtering process can be written as a convolution of the observed fields. As presented in Appendix and section 4, our combined estimator is unbiased, and equally optimal as the OQDE for Gaussian sources, and has better performance for non-Gaussian sources, and recovers three extra (constant) modes.

Other authors also developed reconstruction methods from alternative approaches. Benton Metcalf & White (2006) give a estimator for shear. They choose the separate 2-D slices at certain redshift intervals, and then these slices can be treated as independent samples for the same lensing structure. As a result, the information between these slices are lost. Cooray (2004) expands the lensed field to a higher order of the gravitational potential, and investigates the higher order correction to the lensed power spectrum.

The paper is organized as follows: The basic framework of lensing and the reconstruction method is introduced in §2. The numerical methods are presented in §3. The results are discussed in §4. We conclude in §5.

## 2 LENSING AND RECONSTRUCTION

Photons are deflected by clumpy matter when they propagate from the source to the observer. This effect can be used to map the mass distribution if we can measure the distortion of an image. In this section, we will first review the lensing theory, which serves to define our notation. We then develop an optimal quadratic estimator using a maximum likelihood method. The reconstruction depends on the power spectrum of the source. The noise and normalization of the reconstruction are calculated in the appendix.

### 2.1 Lensing

The Jacobian matrix describing the mapping between the source and image planes is defined as

$$\mathbf{J}(\boldsymbol{\theta}, \chi) = \frac{1}{f_K(\chi)} \frac{\partial \mathbf{x}}{\partial \boldsymbol{\theta}}. \quad (1)$$

Here  $\chi$  is the radial coordinate, and  $f_K(\chi)$  is the comoving angular diameter distance. We consider a ray bundle intersecting at the observer and denote  $\mathbf{x}(\boldsymbol{\theta}, \chi)$  as the comoving transverse coordinate of a ray.

In the lensing literature, the physical quantities frequently used to describe a lensing field are convergence  $\kappa$  and shear  $\gamma$ , which are given by

$$\mathbf{J}(\boldsymbol{\theta}, \chi) = \begin{pmatrix} 1 - \kappa - \gamma_1 & -\gamma_2 \\ -\gamma_2 & 1 - \kappa + \gamma_1 \end{pmatrix}.$$

Equivalently, the convergence and shear can also be written as  $\kappa = (\Phi_{,11} + \Phi_{,22})/2$ ;  $\gamma_1 = (\Phi_{,11} - \Phi_{,22})/2$ ;  $\gamma_2 = \Phi_{,12}$ .  $\Phi$  is the projected 2-D potential:

$$\Phi = \frac{2}{c^2} \int_0^\chi d\chi' \frac{f_K(\chi') f_K(\chi - \chi')}{f_K(\chi)} \phi[f_K(\chi') \boldsymbol{\theta}(\chi'), \chi']. \quad (2)$$

Here subscripts '1' and '2' refer to the derivative to the two perpendicular transverse coordinates, and  $\phi$  is the 3-D Newtonian gravitational potential. Note that the integral is along the actual perturbed path of each photon. In the Born approximation, the deflection is approximated by an integral along the unperturbed path.

In the small angle approximation (Limber 1954),  $\nabla_\perp^2$  can be replaced by  $\nabla^2$  in the integral. We get the Limber equation

$$\kappa = \frac{3H_0^2}{2} \Omega_m \int_0^\chi d\chi' g(\chi', \chi) \frac{\delta}{a(\chi')}, \quad (3)$$

with  $g(\chi', \chi) = f_K(\chi')f_K(\chi - \chi')/f_K(\chi)$ .  $\Omega_m$  is the mass density parameter,  $H_0$  is the current Hubble constant,  $a$  is the scale factor, and  $\delta$  is the over-density.

Kaiser (1992) derived the Fourier-space version of the Limber equation

$$P_\kappa(l) = \frac{9}{4} \left( \frac{H_0}{c} \right)^4 \Omega_m^2 \int_0^{\chi_H} d\chi \frac{g^2(\chi)}{a^2(\chi)} P \left( \frac{l}{f_K(\chi)}, \chi \right). \quad (4)$$

Here  $P_\kappa(l)$  is the 2-D power spectrum of the  $\kappa$  field,  $P(l/f_K(\chi), \chi)$  is the 3-D power spectrum of matter, and  $\chi_H$  is the comoving distance to the Hubble horizon. The equation is valid when the power spectrum  $P_\kappa$  evolves slowly over time corresponding to the scales of fluctuation of interest, and these fluctuation scales are smaller than the horizon scale.

## 2.2 Reconstruction of large-scale structure

We first heuristically review the quadratic lensing estimation in two dimensions. Then we will proceed with a generalization to 3-D with a quantitative derivation.

Lensing will change the distribution of a temperature field by changing length scales. Lensing estimation relies on statistical changes to quadratic quantities in the source plane temperature field. We use a tilde to denote a lensed quantity. All estimators work by convolving the temperature field with a window,

$$\tilde{T}_1(\mathbf{x}) = \int d^2x' \tilde{T}(\mathbf{x}') W_1(\mathbf{x} - \mathbf{x}'), \quad (5)$$

and a second window

$$\tilde{T}_2(\mathbf{x}) = \int d^2x' \tilde{T}(\mathbf{x}') W_2(\mathbf{x} - \mathbf{x}'). \quad (6)$$

The quadratic estimator is simply the product of the two convolved temperature fields,

$$E(\mathbf{x}) \equiv \tilde{T}_1(\mathbf{x}) \tilde{T}_2(\mathbf{x}). \quad (7)$$

In the weak lensing case, the estimator is a linear function of the weak lensing parameters  $(\kappa, \gamma)$ . The simplest case is two equal, azimuthally symmetric window functions  $W_1 = W_2 = f(r)$ . Considering the limit that  $\kappa$  is a constant value, the estimator is linearly proportionate to  $\kappa$ :

$$\langle E \rangle \propto \kappa + V, \quad (8)$$

and  $V$  is the mean covariance. Here  $\langle \dots \rangle$  means ensemble average. For a stochastic random field, the ensemble average can be calculated by the volume average if the volume is big enough. We can absorb  $V$  as well as the normalization coefficient into  $E$  for convenience, i.e.,  $E(\mathbf{x}) \equiv \tilde{T}_1(\mathbf{x}) \tilde{T}_2(\mathbf{x}) - V$ . When  $\kappa$  is spatially variable,  $E$  needs to be normalized by a scale dependent factor  $b(k)$ . This corresponds to a convolution of  $\kappa$  with a kernel:

$$\langle E(\mathbf{x}) \rangle = \int d^2x' \kappa(\mathbf{x}') b(\mathbf{x} - \mathbf{x}'), \quad (9)$$

where kernel  $b$  is the Fourier transform of the normalization factor.

One can optimize the functions to minimize the error on the lensing variables. In this paper we will compare various forms of the smoothing windows, which include as special case the traditional Optimal Quadratic Deflection Estimator. The simplest case is a constant value of  $\kappa$ , for which one can compute its variance

$$\langle \kappa^2 \rangle = \langle (\tilde{T}_1(\mathbf{x})^2) \rangle. \quad (10)$$

Lensing is a small perturbation of the variance, therefore we can calculate the variance from the unlensed source field, i.e.,  $\langle (T_1(\mathbf{x})^2)^2 \rangle \approx \langle (\tilde{T}_1(\mathbf{x})^2)^2 \rangle$ . Performing a variation to minimize the variance, one can find the optimal window function. It turns out that the window functions do not depend on the spatial structure of the lensing field. Only the normalization factor  $b$  in Eq. (9) is scale dependent. We solve the optimal window function at scales where the constant  $\kappa$  approximation works well, and the solution should also be optimal for other scales.

Shear and deflection angles are tensorial and vectorial quantities and require anisotropic or vectorial choices of the window function

$$\mathbf{E}_\gamma = \tilde{\mathbf{T}}_1 \tilde{\mathbf{T}}_2, \quad \tilde{\mathbf{T}}_1 = \int d^2\theta' \tilde{T}(\theta') \mathbf{W}_1(\boldsymbol{\theta} - \boldsymbol{\theta}'), \quad \tilde{\mathbf{T}}_2 = \int d^2\theta' \tilde{T}(\theta') \mathbf{W}_2(\boldsymbol{\theta} - \boldsymbol{\theta}'), \quad (11)$$

$$\mathbf{E}_d = \tilde{\mathbf{T}}_1 \tilde{\mathbf{T}}_2, \quad \tilde{\mathbf{T}}_1 = \int d^2\theta' \tilde{T}(\theta') \mathbf{W}_1(\boldsymbol{\theta} - \boldsymbol{\theta}'), \quad \tilde{\mathbf{T}}_2 = \int d^2\theta' \tilde{T}(\theta') \mathbf{W}_2(\boldsymbol{\theta} - \boldsymbol{\theta}'). \quad (12)$$

This will be explained in detail in sections 2.2.2 and 2.3.

The source is usually treated as a Gaussian stochastic field in the literature on reconstruction methods. While this is valid

for CMB on large angular scales, 21-cm background sources are not always Gaussian. In this paper we attempt to understand the influence of this non-Gaussianity. Optimal estimators for Gaussian sources are not necessarily optimal for non-Gaussian sources. Here, we will construct the convergence and shear field directly, instead of following the deflection angles or potential field reconstruction in CMB lensing. There are three reasons to do this: Firstly, the strength of lensing is evident through the magnitude of  $\kappa$  or  $\gamma$  since they are dimensionless quantities. The rms deflection angle of photons from 21-cm emission is at the magnitude of a few arcmin, which is comparable to the lensing scales we are resolving. Some authors argued that perturbation theory on the deflection angle will break down at these scales (Cooray 2004; Mandel & Zaldarriaga 2006). However,  $\kappa$  and  $\gamma$  are still small and can still work with perturbation calculations without ambiguity. Secondly,  $\kappa$  and  $\gamma$  have well defined limits as they approach a constant, while only spatially variable deflection angles or potentials can be measured. This significantly simplifies the derivations. Finally,  $\kappa$  and  $\gamma$  are standard variables to use in broader lensing studies, such as strong lensing and cosmic shear. Using the same convention in different subfields will help to generalize the underlying physics of lensing.

The estimators are unbiased, as shown in the appendix. Furthermore, we confirm that our combined estimators from  $\kappa$  and  $\gamma$  have the same optimality as the OQDE for Gaussian sources. When the sources are non-Gaussian, our estimators have better S/N.

### 2.2.1 Maximum likelihood estimator of $\kappa$

We now derive the quantitative window functions for 21-cm lensing reconstruction. Due to their similarity, it is helpful to quickly review the reconstruction in CMB lensing: The early work by Zaldarriaga & Seljak (1999) used the quadratic combination of the derivatives of the CMB field to reconstruct the lens distribution. Since the CMB has an intrinsic Gaussian distribution, The optimal quadratic estimator (Hu 2001b) can also be applied to lensing reconstruction with CMB polarization (Hu & Okamoto 2002). Zahn & Zaldarriaga (2006) generalized the optimal quadratic estimator of CMB lensing to 21-cm lensing.

We will construct estimators for  $\kappa$  and  $\gamma$  with the 21-cm brightness temperature fields, starting from a maximum likelihood method which is consistent with the quadratic minimum variance method when the field is Gaussian. We will show that the OQDE and our approach are the same if the sources are Gaussian, however the problem is simplified in a intuitive way by using the limit that  $\kappa$  and  $\gamma$  vary slowly in small scales.

The magnification is

$$\mu = \frac{1}{(1 - \kappa)^2 - \gamma^2} \sim 1 + 2\kappa. \quad (13)$$

The last approximation is valid since both  $\kappa$  and  $\gamma$  are much smaller than 1 in the weak lensing regime.

We use Bayesian statistics and assume the prior distribution of parameter  $\kappa$  to be flat. For a  $M$  pixel map on the sky, the posterior likelihood function of the source field has a Gaussian distribution, and can be written as

$$\mathcal{P}(\tilde{T}(\mathbf{k})) = (2\pi)^{-M/2} \det(\mathbf{C}_{\tilde{T}\tilde{T}})^{-1/2} e^{-\frac{1}{2} \tilde{T}^\dagger \mathbf{C}_{\tilde{T}\tilde{T}}^{-1} \tilde{T}}. \quad (14)$$

Here  $\tilde{T} = \tilde{T}_b + n$  is the brightness temperature of the diffusive 21-cm emission lensed by the large-scale structure plus measurement noise. To simplify the algebra, we use the negative logarithm  $\mathcal{L}$  of the likelihood function in our calculation,

$$\mathcal{L} = -\ln \mathcal{P} = \frac{1}{2} \tilde{T}^\dagger \mathbf{C}_{\tilde{T}\tilde{T}}^{-1} \tilde{T} + \frac{1}{2} \ln \det \mathbf{C}_{\tilde{T}\tilde{T}}. \quad (15)$$

Here  $\tilde{T}$  is the 3-D discrete Fourier transform of measured temperature.  $\mathbf{C}_{\tilde{T}\tilde{T}} = \mathbf{C}_S + \mathbf{C}_N$  is the covariance matrix, and the signal contribution  $\mathbf{C}_S$  and noise contribution  $\mathbf{C}_N$  are both diagonal in Fourier space and uncorrelated to each other. In the continuum limit, the likelihood function can be written as

$$\mathcal{L} = \frac{1}{4\pi^2} \left[ \int d^3k \ln \tilde{P}_{3D}^{\text{tot}}(\mathbf{k}) + \int d^3k \frac{|\tilde{T}(\mathbf{k})|^2}{\tilde{P}_{3D}^{\text{tot}}(\mathbf{k})} \right]. \quad (16)$$

We use  $\tilde{P}_{3D}^{\text{tot}} = \tilde{P}_{3D}(\mathbf{k}) + P_N(\mathbf{k})$  to represent signal plus noise power spectrum in the following text, where  $\tilde{P}_{3D}(\mathbf{k})$  is 3-D power spectrum of the distorted 21-cm field, and  $P_N(\mathbf{k})$  is the noise power spectrum. The dimensionless power spectrum of the 3-D 21-cm gas slices can be written as

$$\Delta_{3D}^2(k) = \frac{k^3}{2\pi^2} P_{3D}(k), \quad (17)$$

where  $k = |\mathbf{k}|$  since the gas is statistically isotropic.

The geometry of the 21-cm field will be changed by the lensing:

$$\tilde{T}_b(\mathbf{k}_\perp, k_\parallel) = \int d^3x \tilde{T}_b(\mathbf{x}) e^{-i\mathbf{k}\cdot\mathbf{x}} = \int d^2x_\perp \int dx_\parallel T_b((1 - \kappa)\mathbf{x}_\perp, x_\parallel) e^{-i(\mathbf{k}_\perp \cdot \mathbf{x}_\perp + k_\parallel x_\parallel)} = \frac{1}{(1 - \kappa)^2} T_b((1 + \kappa)\mathbf{k}_\perp, k_\parallel), \quad (18)$$

where ' $\perp$ ' and ' $\parallel$ ' mean the perpendicular and parallel direction of the line-of-sight respectively. We ignore the contribution of shear first. Then the length scale is magnified on the transverse plane by a factor  $\kappa$ . Isotropy is broken in 3-D but is still conserved on the 2-D cross section. The statistical properties of the 21-cm field will be changed by the lensing, i.e., the power spectrum will also change:

$$\langle \tilde{T}_b^*(\mathbf{k}_\perp, k_\parallel) \tilde{T}_b(\mathbf{k}'_\perp, k'_\parallel) \rangle = (2\pi)^2 \delta^{2D}(\mathbf{k}_\perp - \mathbf{k}'_\perp) (2\pi) \delta^D(k_\parallel - k'_\parallel) \tilde{P}_{3D}(\mathbf{k}_\perp, k_\parallel). \quad (19)$$

The delta function has the property:

$$\delta^{2D}((1+\kappa)\mathbf{k}_\perp - (1+\kappa)\mathbf{k}'_\perp) = \frac{1}{(1+\kappa)^2} \delta^{2D}(\mathbf{k}_\perp - \mathbf{k}'_\perp). \quad (20)$$

Therefore the relationship between the unlensed and lensed power spectrum is

$$\tilde{P}_{3D}(\mathbf{k}_\perp, k_\parallel) = (1+2\kappa)P_{3D}((1+\kappa)\mathbf{k}_\perp, k_\parallel) = (1+2\kappa)P_{3D}(\sqrt{(1+\kappa)^2 k_\perp^2 + k_\parallel^2}) \approx (1+2\kappa)(P_{3D}(k) + \kappa \Delta P_{3D}), \quad (21)$$

where  $\Delta P_{3D} = P'_{3D} k(k_\perp^2/k^2)$ , and  $P'_{3D}(k) = dP_{3D}(k)/dk$ . The second equivalence is due to the statistical isotropy of the unlensed power spectrum.

Differentiation of the lensed power spectrum gives

$$\frac{\delta \tilde{P}_{3D}(\mathbf{k})}{\delta \kappa} = 2P_{3D} + (1+2\kappa)\Delta P_{3D}, \quad (22)$$

and the maximum likelihood condition requires

$$\frac{\delta \mathcal{L}}{\delta \kappa} \approx \frac{1}{2} L^3 \int \frac{d^3 k}{(2\pi)^3} \frac{(\tilde{P}_{3D}^{\text{tot}} - |\tilde{T}|^2 L^{-3})}{P_{3D}^{\text{tot}^2}} \frac{\delta \tilde{P}_{3D}}{\delta \kappa} = 0, \quad (23)$$

which has the solution

$$E_\kappa = \int \frac{d^3 k}{(2\pi)^3} (|\tilde{T}|^2 L^{-3}) \mathcal{F}^\kappa(\mathbf{k}) - V_\kappa. \quad (24)$$

We have approximated  $\tilde{P}_{3D}^{\text{tot}}$  by  $P_{3D}^{\text{tot}}$  in the denominator of Eq. (23). To simplify the problem, we assume the source is a cube with physical length  $L$  in each dimension. The offset constant  $V_\kappa = \langle \sigma^2 \rangle = \int d^3 k / (2\pi)^3 P_{3D}^{\text{tot}}(\mathbf{k}) \mathcal{F}^\kappa(\mathbf{k})$ , and the optimal filter  $\mathcal{F}^\kappa$  is

$$\mathcal{F}^\kappa(\mathbf{k}) = \frac{2P_{3D}(\mathbf{k}) + \Delta P_{3D}(\mathbf{k})}{P_{3D}^{\text{tot}^2}(\mathbf{k}) Q_\kappa}, \quad (25)$$

with  $Q_\kappa = \int d^3 k / (2\pi)^3 (2P_{3D} + \Delta P_{3D})(\mathbf{k}) \mathcal{F}^\kappa(\mathbf{k})$ .

From Parseval's theorem, we can rewrite Eq. (24) in the form of a convolution of the density field and a window function in real space

$$\int \frac{d^3 k}{(2\pi)^3} \tilde{T}^*(\mathbf{k}) \tilde{T}(\mathbf{k}) \mathcal{F}^\kappa(\mathbf{k}) = \int d^3 x \tilde{T}_{w_1}^\kappa(\mathbf{x}) \tilde{T}_{w_2}^\kappa(\mathbf{x}) = L^2 \int dx_\parallel \tilde{T}_{w_1}^\kappa(\mathbf{x}_\perp, x_\parallel) \tilde{T}_{w_2}^\kappa(\mathbf{x}_\perp, x_\parallel). \quad (26)$$

In Eq. (26) the two window functions are the decomposition of the optimal filter  $W_1^\kappa(\mathbf{k}) W_2^\kappa(\mathbf{k}) = \mathcal{F}^\kappa(\mathbf{k})$ . The last '=' in Eq. (26) holds when  $\kappa$  is constant. One can choose  $W_1^\kappa(\mathbf{k}) = W_2^\kappa(\mathbf{k}) = \sqrt{\mathcal{F}^\kappa}$ . If  $\mathcal{F}^\kappa < 0$ , we choose  $W_1^\kappa = -W_2^\kappa = \sqrt{|\mathcal{F}^\kappa|}$ . The convergence field is equivalent to the covariance of the measured maps with two windows applied. In the slowly spatially varying  $\kappa$  limit, all decomposition into two windows are equivalent. As we will show later, the shear construction can also be represented in the form of the covariance of two filtered temperature maps. These maps will have symmetric Probability Density Function (PDF), which can reduce the non-Gaussianity of the maps so that a better S/N level can be achieved, when the shear window functions are chosen properly. The last two steps in Eq. (26) assumes the fluctuation of the convergence field is slow compared to the filter. Then we can apply the estimator to each beam in the map:

$$E_\kappa(\mathbf{x}_\perp) = L^{-1} \int dx_\parallel \tilde{T}_{w_1}^\kappa(\mathbf{x}) \tilde{T}_{w_2}^\kappa(\mathbf{x}) - V_\kappa, \quad (27)$$

where  $\tilde{T}_{w_1}^\kappa$  and  $\tilde{T}_{w_2}^\kappa$  are the convolution of  $\tilde{T}$  and window function  $W_1^\kappa(\mathbf{x})$  and  $W_2^\kappa(\mathbf{x})$  respectively, which are the real space version of  $W_1^\kappa(\mathbf{k})$  and  $W_2^\kappa(\mathbf{k})$ . The reconstruction of the  $\kappa$  is dominated by the gradient of the power spectrum  $d \ln \Delta^2 / d \ln k$ , which follows the expression of our estimator in Eq. (24).

We can then generalize the estimator to a spatially varying lensing field. In the appendix we show

$$\int d^2 x'_\perp \kappa(\mathbf{x}'_\perp) b_\kappa(\mathbf{x}_\perp - \mathbf{x}'_\perp) = \langle E_\kappa(\mathbf{x}_\perp) \rangle. \quad (28)$$

Equivalently, for smaller scales, we will need to normalize the reconstructed lensing field by a scale dependent factor in Fourier space, which is calculated in the appendix.

$$\hat{\kappa}(\mathbf{l}) = b_\kappa^{-1}(\mathbf{l})E_\kappa(\mathbf{l}) = \kappa(\mathbf{l}) + n(\mathbf{l}) , \quad (29)$$

where  $\mathbf{l} = \mathbf{k}_\perp \chi(z_s)$ , and  $z_s$  is the redshift of the source. Here  $b_\kappa(l)$  is the normalization factor ( $\lim_{l \rightarrow 0} b_\kappa(l) = 1$ ), and  $n(l)$  is the noise, since different Fourier modes are independent. They do not depend on direction because variables related to  $\kappa$  are isotropic on the transverse plane. In the appendix, we show that the normalization factor is unity at small  $l$  when  $Q_\kappa$  has the form as  $Q_\kappa = \int d^3k / (2\pi)^3 (2P_{3D} + \Delta P_{3D})(\mathbf{k}) \mathcal{F}^\kappa(\mathbf{k})$ .

### 2.2.2 Estimator of shear

When shear is taken into account, not only the scale but the directions of the coordinates are changed. We will start the derivation from the constant shear case.

$$\begin{aligned} \tilde{T}_b(\mathbf{k}_\perp, k_\parallel) &= \int d^3x \tilde{T}_b(\mathbf{x}) e^{-i\mathbf{k} \cdot \mathbf{x}} = \int d^2x_\perp \int dx_\parallel T_b(\mathbf{J}\mathbf{x}_\perp, x_\parallel) e^{-i(\mathbf{k}_\perp \cdot \mathbf{x}_\perp + k_\parallel x_\parallel)} \\ &= |\mathbf{J}|^{-1} \int d^2x'_\perp \int dx_\parallel T_b(\mathbf{x}'_\perp, x_\parallel) e^{-i(\mathbf{k}'_\perp \cdot \mathbf{x}'_\perp + k_\parallel x_\parallel)} = |\mathbf{J}|^{-1} T_b(\mathbf{J}^{-1}\mathbf{k}_\perp, k_\parallel) , \end{aligned} \quad (30)$$

here  $d^2x'_\perp = |\mathbf{J}| d^2x_\perp$ ,  $\mathbf{k}'_\perp = \mathbf{J}^{-1}\mathbf{k}_\perp$ . Now the symmetry is broken even on the transverse plane due to the anisotropic distortion caused by the shear.

Since  $\delta^{2D}(\mathbf{J}^{-1}\mathbf{k}) = |\mathbf{J}| \delta^{2D}(\mathbf{k})$ , Eq. (19) implies

$$\tilde{P}_{3D}(\mathbf{k}_\perp, k_\parallel) = |\mathbf{J}|^{-1} P_{3D}(\mathbf{J}^{-1}\mathbf{k}_\perp, k_\parallel) \approx (1 + 2\kappa) [P_{3D}(k) + \Delta P_{3D}(\mathbf{k})(\kappa + \gamma_1 \cos 2\theta_{\mathbf{k}_\perp} + \gamma_2 \sin 2\theta_{\mathbf{k}_\perp})] , \quad (31)$$

where  $\theta_{\mathbf{k}_\perp}$  is the angle between  $\mathbf{k}_\perp$  and the transverse coordinate.

Maximum likelihood requires  $\delta\mathcal{L}/\delta\gamma_1 = 0$ , and  $\delta\mathcal{L}/\delta\gamma_2 = 0$ . The maximum likelihood shear estimators can be written as a tensor  $\mathbf{E}_\gamma$ :

$$E_{\gamma ij} = L^{-1} \int dx_\parallel \tilde{T}_{w_i}^\gamma \tilde{T}_{w_j}^\gamma , \quad (32)$$

where  $\tilde{T}_{w_i}^\gamma$  is convolution of the temperature field with  $W_i^\gamma$ , and  $W_i^\gamma(\mathbf{k}) = (2\Delta P_{3D}/P_{3D}^2 Q_\gamma)^{1/2} \hat{k}_i$ ,  $\hat{k}_i$  ( $i, j = 1, 2$ ) is one of the two unit vectors on the transverse plane. When  $\Delta P < 0$ , we can choose  $W_1^\gamma = |2\Delta P_{3D}/P_{3D}^2 Q_\gamma|^{1/2} \hat{k}_1$ ,  $W_2^\gamma = -|2\Delta P_{3D}/P_{3D}^2 Q_\gamma|^{1/2} \hat{k}_2$ . The normalization factor  $Q_\gamma = \int d^3k / (2\pi)^3 \Delta P_{3D}(\mathbf{k}) \hat{k}_1 \hat{k}_2 W_1^\gamma(\mathbf{k}) W_2^\gamma(\mathbf{k})$ . The two components of shear are now:

$$\hat{\gamma}_1 = E_{\gamma 12} = E_{\gamma 21}, \quad \hat{\gamma}_2 = \frac{E_{\gamma 11} - E_{\gamma 22}}{2} . \quad (33)$$

Note that there is a difference between the reconstruction for convergence and shear. Shear reconstruction depends on the gradient of  $P(k)$ , while convergence reconstruction depends on the gradient of  $\Delta^2(k)$  in a 2-D analogue. To test our method, we can generate a Gaussian source field with power law power spectrum  $P(k) = k^\beta$ . In the 2-D analogue case, the convergence field can not be measured if  $\beta = -2$ , because the variance is conserved. However in 3-D, when  $\beta = -3$ , the convergence field can still be measured, which is due to the more complicated shape of the window function in 3-D. When  $\beta = 0$ , the shear can not be measured in either 2-D or 3-D.

In analogy to  $\kappa$  reconstruction, we can calculate the normalization factors  $b_{\gamma_1}$  and  $b_{\gamma_2}$ . The calculations for the normalization factors and noise are presented in the appendix.

## 2.3 The combined estimator and the OQDE

The combined estimator of  $\kappa$  can be written as

$$\hat{\kappa}_{\text{comb}}(\mathbf{l}) = \frac{\hat{\kappa}(\mathbf{l}) N_\kappa(\mathbf{l})^{-1} + \hat{\gamma}_E(\mathbf{l}) N_{\gamma_E}(\mathbf{l})^{-1}}{N_\kappa(\mathbf{l})^{-1} + N_{\gamma_E}(\mathbf{l})^{-1}} , \quad (34)$$

where  $\hat{\gamma}_E$  is the convergence constructed from shear field,

$$\hat{\gamma}_E(\mathbf{l}) = \hat{\gamma}_1(\mathbf{l}) \cos 2\theta_l + \hat{\gamma}_2(\mathbf{l}) \sin 2\theta_l , \quad (35)$$

and  $\theta_l$  is the angle of  $\mathbf{l}$ .

The 2-D OQDE in CMB lensing can be written as product of two filtered temperature field (Hu 2001b; Lewis & Challinor 2006). Furthermore, the 3-D OQDE can be written in the same form of Eq. (12), though it is not explicit (private communication with Oliver Zahn).

$$\mathbf{E}_d(\theta) = L^{-1} \int dx_\parallel T_1(\theta, x_\parallel) T_2(\theta, x_\parallel) , \quad (36)$$

and

$$\int d^2\theta' \mathbf{d}(\theta') b_{\text{d}}(\boldsymbol{\theta} - \boldsymbol{\theta}') = \langle E_{\text{d}}(\boldsymbol{\theta}) \rangle. \quad (37)$$

$b_{\text{d}}$  is a normalization factor,  $\mathbf{T}_1 = \int d^2\theta' T(\boldsymbol{\theta}') \mathbf{W}_1(\boldsymbol{\theta} - \boldsymbol{\theta}')$  and  $T_2 = \int d^2\theta' T(\boldsymbol{\theta}') W_2(\boldsymbol{\theta} - \boldsymbol{\theta}')$  are convolved temperature fields, where the window functions are Fourier transforms of:

$$\begin{aligned} \mathbf{W}_1(\mathbf{l}, k_{\parallel}) &= \frac{-i\mathbf{l}P_{3\text{D}}(\mathbf{l}, k_{\parallel})}{\bar{P}_{3\text{D}}^{\text{tot}}(\mathbf{l}, k_{\parallel})}, \\ W_2(\mathbf{l}, k_{\parallel}) &= \frac{1}{\bar{P}_{3\text{D}}^{\text{tot}}(\mathbf{l}, k_{\parallel})}. \end{aligned} \quad (38)$$

We note that the OQDE and our estimators have the same form. The contribution from lensing in Eq. (10) is secondary, and the noise of reconstruction is mainly determined by the unlensed terms. Therefore we can measure the numerical reconstruction noise without lensing the sources.

### 3 NUMERICAL METHODS

#### 3.1 Simulation

The fluctuation in the 21-cm brightness temperature may depend on many factors, such as the gas density, temperature, neutral fraction, radial velocity gradient and Ly  $\alpha$  flux (Barkana & Loeb 2005). In our work, we do not consider the redshift space distortion effect caused by the non-zero radial peculiar velocity gradient, and simply assume the brightness temperature is proportional to the density of the neutral gas.

$$T_b \approx (27\text{mK}) \left( \frac{1+z}{10} \right)^{1/2} \frac{T_s - T_{\text{CMB}}}{T_s} (1 + \delta_{\text{HI}}), \quad (39)$$

where  $T_b$  is the brightness temperature increment respective to CMB,  $T_s$  is the spin temperature, which is about to be much bigger than  $T_{\text{CMB}}$ , and  $\delta_{\text{HI}}$  is the over-density of the neutral hydrogen.

Our work mainly focuses on the non-Gaussian aspect and 3-D properties of the reconstruction, and these effects also exist in a pure dark matter distribution. The neutral gas will trace the total mass distribution, which is dominated by the dark matter haloes. A simplification is to use the dark matter as the source directly. Even though this will bring some bias at small scales, the approximation is valid at large scales. The dark matter distributions are generated using the PMFAST code (Merz et al. 2005).

The high resolution PMFAST simulation was performed on a  $1456^3$  fine mesh with  $3.9 \times 10^8$  particles. The production platform was the IA-64 'lobster' cluster at CITA, which consists of 8 nodes. One of them was upgraded, so we have used the remaining 7 nodes. Each node contains four 733 MHz Itanium-1 processors and 64 GB RAM. The simulation started at an initial redshift  $z_i = 100$  and ran for 63 steps with comoving box-size  $L = 50h^{-1}$  Mpc. The initial condition was generated using the Zeldovich approximation, and the matter transfer function was calculated using CMBFAST (Seljak & Zaldarriaga 1996). The cosmological parameters were chosen in accordance with the WMAP result (Spergel 2003):  $\Omega_{\text{m}} = 0.27$ ,  $\Omega_{\Lambda} = 0.73$ ,  $\Omega_b = 0.044$ ,  $n = 1.0$ ,  $\sigma_8 = 0.84$ , and  $h_0 = 0.71$ . 20 independent boxes were generated. We had 3-D data at  $z = 7$  at hand, and used them in our numerical tests for convenience.

#### 3.2 Convergence and shear map construction

The dimensionless power spectrum, which is the contribution to the variance of over-density per logarithmic interval in spatial wave number, can be measured from the source data in the periodic simulation box.

To reduce the computation time, our numeric results on the reconstruction use a re-sampled distribution. We will generate 20 independent sources each on  $512^3$  grids, to investigate the statistics. The total co-moving length along the line-of-sight of 20 simulation boxes is  $1h^{-1}$  Gpc, which is about the same size as the observable 21-cm region distributed between redshifts 10 – 20. The correlation between the boxes can be ignored since the box-size is much larger than the non-linear length scale, and the number of neglected modes is small. In Fig. 1, the solid line is the power spectrum of the re-sampled sources. To measure the dependence of non-Gaussianity on scale, we compare the results with different scales of experimental noise cut off.

We simply assume the noise to be zero above a cut off and infinity below the cut off scale. This is a reasonable approximation for a filled aperture experiment, which has good brightness sensitivity, and an exponentially growing noise at small scales. Three cut off were chosen at  $k_c = 1h \text{ Mpc}^{-1}$ ,  $4h \text{ Mpc}^{-1}$ ,  $16h \text{ Mpc}^{-1}$ , which represent the linear, quasi-linear and non-linear scales. Three different experimental noise levels are shown as vertical lines in Fig. 1.

In principle, the convergence map is the variance (or covariance when the filter  $\mathcal{F}^{\kappa}$  has negative value) of the over-density

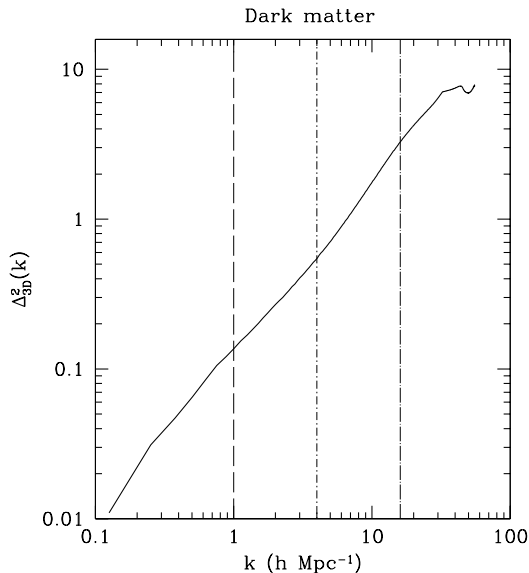


**Figure 1.** The dimensionless power spectra of the re-sampled dark matter from the  $1456^3$  N-body simulation in three dimensions are given. The solid line is the power spectrum on the  $512^3$  grids. The re-sampled sources keep the non-linearity and the non-Gaussianity of the structures up to  $k \sim 30h \text{ Mpc}^{-1}$ . Three different experimental noise cut offs are shown with  $k_c = 1h \text{ Mpc}^{-1}, 4h \text{ Mpc}^{-1}, 16h \text{ Mpc}^{-1}$ , which represent the linear, quasi-linear and non-linear scales.

field after a specified filtering process. Shear is the covariance of two maps, since the anisotropic filter can not be factored in to a perfect square. We need to smooth the maps to extract the lensing signal with maximum S/N. The window function used to smooth the lensed map, which is isotropic in the transverse directions to the line-of-sight, can be calculated with Eq. (25). The gradient of the power spectrum becomes negative at small scales; that comes from the limited resolution of the N-body simulation and is unphysical. The experimental noise will put a natural cut off at small scales.

As mentioned in Section 2.2.2, the reconstruction of  $\kappa$  will depend on  $2P + \Delta P$ , in 2-D which is equivalent to the gradient of 2-D version of  $\Delta_{2D}^2 = k^2 P_{2D}(k)/2\pi$ . In 3-D, it is more complicated since  $\Delta P(\mathbf{k})$  is not isotropic. The optimal window functions have two parts  $W_1$  and  $W_2$ , the choice of which is not unique. One might expect a symmetric decomposition to have the best S/N. The optimal filter of  $\kappa$  is positive except at a few modes, and can be decomposed in to two equivalent parts (one part need to contain a minus sign for those negative value of the filter). In contrast to  $\kappa$ , the shear construction needs to use the covariance between two different windowed temperature fields, since there is a sin or cos component in the window function. The window is a function of the transverse and parallel components of  $\mathbf{k}$ .

We can calculate the mean covariance of the two smoothed maps along the redshift axis for each pixel. From Eq. (27) we can construct the convergence map. Shear maps are reconstructed in the same way, except different optimal window functions are used. The anisotropic part  $\cos 2\theta_{\mathbf{k}_\perp}$  can be decomposed into  $\cos \theta_{\mathbf{k}_\perp} - \sin \theta_{\mathbf{k}_\perp}$  and  $\cos \theta_{\mathbf{k}_\perp} + \sin \theta_{\mathbf{k}_\perp}$ . Both windows can generate a field with even PDF so that the distribution is less non-Gaussian. This is consistent with the numerical results as shown in Fig. 6. Using these two maps, we construct the  $\gamma_1$  map with their covariance, as shown in the Eq. (33). Similarly we can get the  $\gamma_2$  map.

#### 4 NUMERICAL RESULTS AND DISCUSSION

Cooray (2004) claims that the variance will not vary considerably and is not a ideal measurement of the lensing signal. Even though the  $\kappa$  field itself is only a few percent, the integrated effect from the 3-D images will reduce the noise ratio significantly to uncover the signal. Zahn & Zaldarriaga (2006) solve the problem from an alternative approach by generalizing the minimum variance quadratic estimator (Hu & Okamoto 2002) in CMB lensing to 3-D.

A related work was done in Benton Metcalf & White (2006), where they also construct quadratic estimators of shear and convergence in real space, even though they did not include the correlation between the 2-D slices along the line-of-sight and they did not choose the estimator with minimized noise.



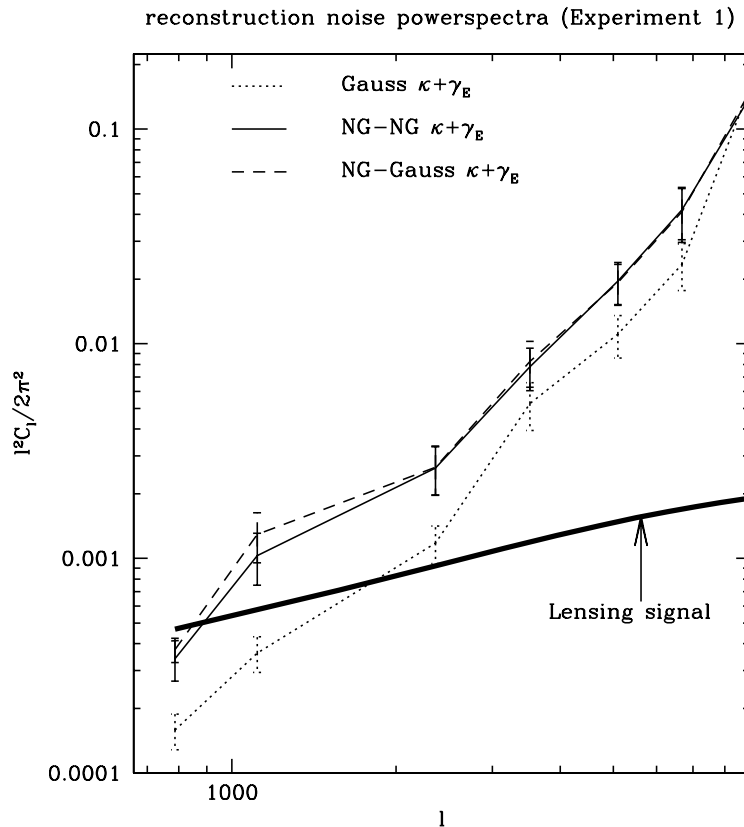


**Figure 2.** The noise of lensing maps from different estimators using experimental noise 1, which cuts off at  $k_c = 1h \text{ Mpc}^{-1}$ . We treat the  $1h^{-1} \text{ Gpc}$  space of gas at  $z = 10 - 20$  as 20 independent sources each is a  $50h^{-1} \text{ Mpc}$  box-size cube. Structures at these redshifts are similar to those at  $z = 7$  used by us, though less non-linear. We can expect to see similar non-Gaussianity effects in the reconstruction with the  $1h^{-1} \text{ Gpc}$  space except that the non-Gaussianity of sources will be smaller. The curves are truncated at  $\sqrt{2}k_c$ , where the noise goes to infinity. The thick solid line is the expected lensing signal. The dotted line is the lensing reconstruction noise for a simulated Gaussian source with the same power spectrum. The dashed curve is the noise from the N-body simulation using the Gaussian estimator, which increases modestly compared to the Gaussian source. It is identical for the optimal  $\kappa, \gamma$  reconstruction as it is for the deflection angle. The thin solid line is noise when shear and convergence are re-weighted by their non-Gaussian variances.

#### 4.1 Non-Gaussianity

The dark matter distribution is linear at large scales, and can be treated as Gaussian. In the non-linear scales, when the amplitude of density fluctuations is big, the structure becomes highly non-Gaussian. Reference Gaussian sources with identical power spectrum to the dark matter are generated.

We treat the  $1h^{-1} \text{ Gpc}$  region at  $z = 10 - 20$  as 20 independent sources. Structures at these redshifts are similar to those at  $z = 7$  used by us, though less non-linear. We can expect to see similar non-Gaussianity effects in the reconstruction with the  $1h^{-1} \text{ Gpc}$  space except that the non-linear scale is smaller. We compare the reconstruction noise with three different experimental noise as well as the lensing signal in Fig. 2, 3 and 4. The thick solid line in the middle panel is the lensing power spectrum, which is calculated with the Limber integral of the 3-D power spectrum of dark matter using Eq. (4). We use the publicly available code Halofit.f (Smith et al. 2003) to generate the nonlinear dark matter power spectrum. The code provides both their fitting results, and the results using the Peacock-Dodds formula (Peacock & Dodds (1996), PD96 hereafter). The ‘stable clustering’ assumption of PD96 breaks down at low redshifts, but is reasonably good at high redshifts where the power spectrum is more linear. The halofit code fits the power spectrum at low redshift to Virgo and GIF CDM simulations, which used the transfer function of Efstathiou et al. (1992). We use a combination of the two: Halofit power spectra are used for redshifts lower than  $z = 3.0$ , and PD96 power spectra are used for higher redshifts.

Since the reconstruction noise of  $\kappa$  is isotropic, one can always choose the direction of the lensing mode  $\mathbf{l}$  to be parallel with a coordinate axis. In this direction,  $\gamma_1(\mathbf{l}) = \kappa(\mathbf{l})$ ,  $\gamma_2(\mathbf{l}) = 0$ , and  $\gamma_E = \gamma_1$ , which simplifies the numerical calculation. The optimal combined estimator becomes the sum of  $\kappa$  and  $\gamma_E$  weighted by their noise. The weights could be the Gaussian  $\kappa, \gamma_E$  noise, or non-Gaussian noise. We will show that the combined estimator with Gaussian noise weights has the same noise as

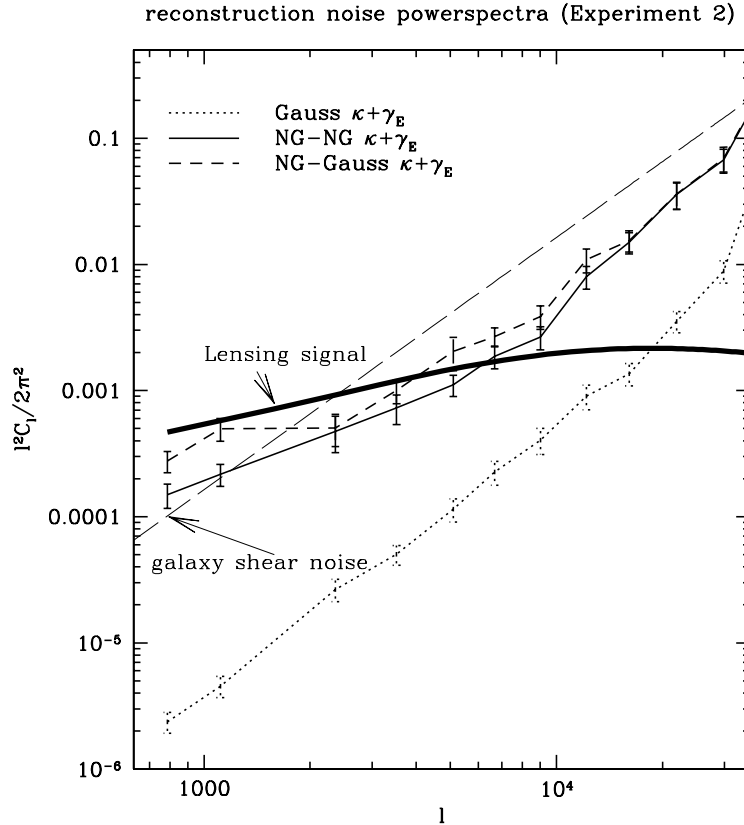


**Figure 3.** Same of Fig. 2, but with cut off at the quasi-linear scales  $k_c = 4h \text{ Mpc}^{-1}$ . The effect of non-Gaussianity of sources is more pronounced. We can compare the S/N with a fiducial cosmic shear survey of sources in the same  $10 < z < 20$  redshift range, which reconstructs the lensing from the shape of galaxies, with a surface density of  $14 \text{ arcmin}^{-2}$ . To map the lensing to the same S/N with redshift  $z \sim 1$  sources requires a density of  $56 \text{ arcmin}^{-2}$  (Hu & White 2001) with rms ellipticity of 0.4. We see that proposed optical lensing surveys are unlikely to outperform 21-cm sources.

the OQDE for both Gaussian and non-Gaussian sources. Fig. 2, 3, and 4 are results using noise cut offs from experiment 1, 2 and 3. The curves are truncated at  $\sqrt{2}k_c$ . The non-Gaussianity increased the noise of all estimators. The first cut off falls in the linear regime, where the non-Gaussianity only has a modest effect on the noise. The second cut off is at the quasi-linear scale. Here the non-Gaussianity increases the noise of the OQDE by about 1 to 2 orders of magnitude. At the highly non-linear scales, the non-Gaussian noise is about 3 to 4 magnitude higher than the Gaussian noise, and in fact higher than that for the more noisy experiment.

Our estimators were derived in the limit that  $\kappa$  and  $\gamma$  are constant, and are optimal in that limit. For spatially variable lens, we solve for the required normalization factors. In the OQDE, the windows do not depend on the scale of the lens, so one might guess the same Ansatz to hold for the  $(\kappa, \gamma)$  estimators. We verify this numerically in Fig. 5. The solid line and dotted line is for Gaussian sources and non-Gaussian sources respectively. The differences are less than a few percent, and consistent with integration errors from the tabulated power spectrum, and most importantly, independent of scale, as we had expected. We do note, that for a finite size survey, the  $(\kappa, \gamma)$  recover the constant mode, which is lost in the OQDE. Three more numbers are recovered.

The combined estimator with  $\kappa$  and  $\gamma_E$  weighted by non-Gaussian noise is more optimal than weighted by Gaussian noise, therefore has lower noise than the OQDE. In fact, the non-Gaussian noise of  $\gamma_E$  is much smaller than  $\kappa$ . To investigate the origin of this change, we first investigate the cause of the increased noise in non-Gaussian sources for  $\kappa$ . This could be because either the non-Gaussianity leads to a high kurtosis in  $\kappa$ , which boosts the errors; or the non-Gaussianity may lead to correlations between modes, resulting in a smaller number of independent modes, and thus a larger error.

In Fig. 6, the PDF of maps smoothed with the  $\kappa$  window are shown. The top, middle and bottom panel show the results with experimental noise cut offs 1, 2 and 3. The solid line is the PDF for maps smoothed with  $\kappa$  window ( $T_1^\kappa, T_2^\kappa$  in section 2.2.1). Because the window functions are almost symmetric, we plot only one PDF. To see the full dynamic range on the x-axis, we plot  $\pm|T|^{1/4}$  as x-axis, and  $\text{PDF}(|T|^{1/4})|T|^{15/4}$  as the y-axis. The integral of the x-axis weighted by the y-axis will

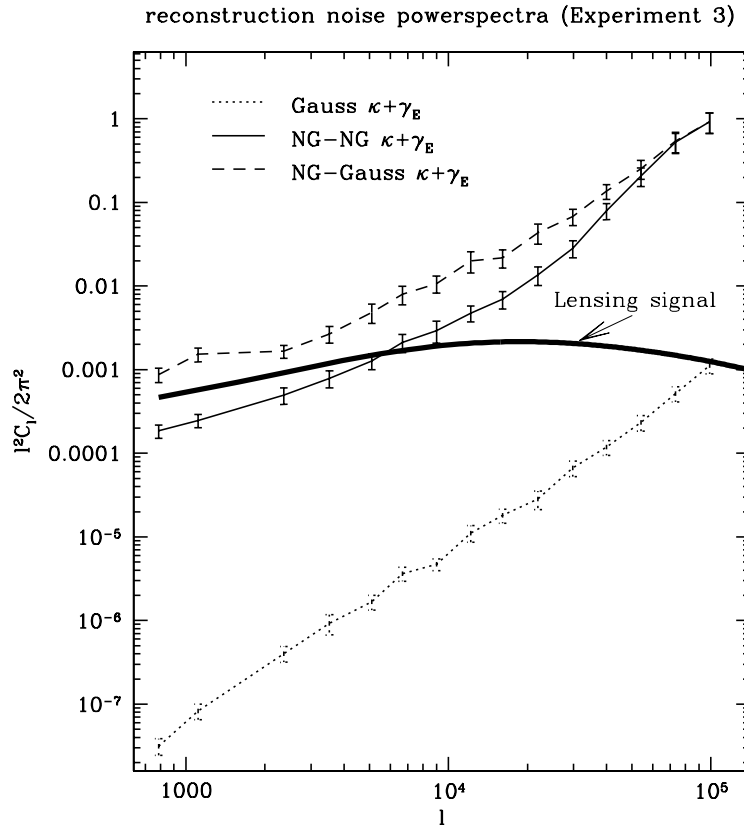


**Figure 4.** Same of Fig. 2, but with cut off at the non-linear scales  $k_c = 16h \text{ Mpc}^{-1}$ . At the highly non-linear scales, the non-Gaussian noise is about 3 to 4 magnitude higher than the Gaussian noise. The combined re-weighted estimator (NG-NG  $\kappa + \gamma_E$ ) has noise about half an order of magnitude lower than the OQDE.

give  $\langle T^4 \rangle$ , which is basically a estimation of the point-wise non-Gaussian reconstruction noise. Here  $\text{PDF}(|T|^{1/4})$  is the PDF of  $|T|^{1/4}$ . To compare with a Gaussian distribution, dotted lines are also plotted. The contributions to the  $\langle T^4 \rangle$  in experiment 1 mainly come from small fluctuation regions. In experiment 2, the large outliers play a more important role but one can still expect the curve to converge. In experiment 3, most contributions come from rare regions with high fluctuations. Caution should be exercised in the interpretation of the most non-linear scales, since a larger number of source samples may result in a different error. It is clear, however, that the noise has increased dramatically.

The kurtosis of  $\kappa$  is  $\langle (T_1^\kappa)^4 \rangle / \langle (T_1^\kappa)^2 \rangle^2 - 3$ , and an analogous quantity can be defined by  $\langle (T_1^\gamma T_2^\gamma)^2 \rangle / (\langle (T_1^\gamma)^2 \rangle \langle (T_2^\gamma)^2 \rangle) - 1$  for shear.  $T_1^\kappa \approx T_2^\kappa$ , and  $T_1^\gamma$  is uncorrelated with  $T_2^\gamma$ . The noise of  $\kappa$  and  $\gamma$  is determined by both kurtosis and number of independent cells. For experimental noise 1, the kurtosis of  $T^\kappa$  and  $T^\gamma$  are 1.2 and 0.29 respectively. The effectively independent cube cells for  $\kappa$  and  $\gamma$  have side length  $4.8h^{-1} \text{ Mpc}$  and  $4.6h^{-1} \text{ Mpc}$  respectively. The corresponding Gaussian sources with the same cut off have effective cell size  $3.0h^{-1} \text{ Mpc}$  and  $3.5h^{-1} \text{ Mpc}$ . For experimental noise 2, the kurtosis of  $T^\kappa$  and  $T^\gamma$  are 18 and 5.7 respectively. The effective cell size for  $\kappa$  and  $\gamma$  are  $1.8h^{-1} \text{ Mpc}$  and  $1.5h^{-1} \text{ Mpc}$  respectively. The corresponding Gaussian sources with the same cut off have effective cell size  $1.0h^{-1} \text{ Mpc}$  and  $1.1h^{-1} \text{ Mpc}$ . For experimental noise 3, the kurtosis for  $T^\kappa$  and  $T^\gamma$  are  $1.6 \times 10^3$  and  $3.5 \times 10^2$  respectively. The effective cell size for  $\kappa$  and  $\gamma$  are  $540h^{-1} \text{ Kpc}$  and  $310h^{-1} \text{ Kpc}$  respectively. The corresponding Gaussian sources with the same cut off have effective cell size  $240h^{-1} \text{ Kpc}$  and  $290h^{-1} \text{ Kpc}$ . We conclude that the shear measurements have lower non-Gaussian noise both because of a smaller point-wise kurtosis, and less correlation between modes.

We will see later that experiment 2 has the largest S/N, which is larger than unity for  $l \lesssim 6000$ . We can compare the S/N with cosmic shear surveys, which reconstruct lensing from the shape of galaxies. The noise can be estimated by  $\langle \gamma^2 \rangle / n_{\text{eff}}$  (Hoekstra et al. 2006; Hu & White 2001), where we use  $\langle \gamma^2 \rangle^{1/2} \approx 0.4$  as the rms intrinsic ellipticity, and  $n_{\text{eff}}$  is the effective number density of galaxies. We plot the shear noise from a survey of sources in the same redshift range  $10 < z < 20$  in Fig. 3, with a surface density of  $14 \text{ arcmin}^{-2}$ . For more realistic source redshifts  $z \sim 1$  in proposed optical surveys (Hu & White 2001), this corresponds to a surface density of  $56 \text{ arcmin}^{-2}$ . In the CFHTLS wide survey the source galaxies are distributed

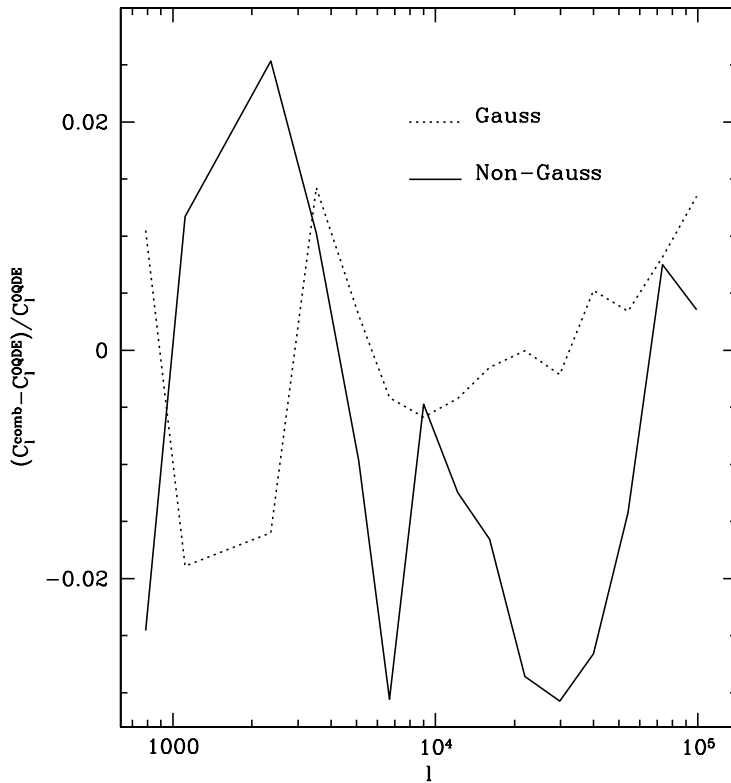


**Figure 5.** The comparison of reconstruction noise from the combined  $(\kappa, \gamma)$  estimator and the OQDE. While the optimality is only proved at low  $l$ , we find them equally optimal for Gaussian sources at all scales. The scatter is consistent with numerical integration errors from the tabulated power spectrum.

at redshifts lower than 3, and their effective number density is  $\sim 12$  galaxies arcmin $^{-2}$  (Hoekstra et al. 2006). This noise is larger still. Even though non-Gaussian 21-cm lensing saturates lensing reconstruction, it still measures more modes than current proposed optical surveys.

In Fig. 7, we show the reconstruction noise at two different  $l$  versus various experimental noise cut off  $k_c$ . The top panel is for the fundamental mode in the box,  $l_1 = 2\pi/L = 783$ , and the bottom panel is for  $l_2 = 6l_1 = 4715$ . As shown in the plot, it is clear that the noise of a Gaussian source decreases as  $k_c$  increases, because of the increasing number of independent modes. The dotted lines are a least squares fitting power law  $N_0 k_c^{-3}$  to the Gaussian noises, and  $N_0 = 3.1 \times 10^{-2}, 1.3 \times 10^{-1}$  for top and bottom panels respectively. This comes from counting the number of available source modes. The dashed lines connect the non-Gaussian noises of the OQDE. The triangles are the reconstruction noise for the combination estimator, which is equal to the OQDE at larger scale  $k_c$  and about half an order of magnitude lower at smaller scales of  $k_c$ . From this plot, we can see that experiment with lower noise does not necessarily decrease the reconstruction noise of the OQDE for non-Gaussian sources. And the experimental noise has a limit around the quasi-linear scale where the OQDE achieves its best S/N. The S/N achieves its maximum around  $k_c^{\text{NG}} \approx 4h \text{ Mpc}^{-1}$ . This cut off with maximum S/N varies only slowly with  $l$ .

If one wants to estimate the effective number of available lensing modes, we can derive an effective cut off of a Gaussian field which gives the same S/N as the optimal non-Gaussian sources estimator. This is  $k_c^{\text{G}} \approx 2h \text{ Mpc}^{-1}$ , where the power spectrum of source is  $\Delta^2 \approx 0.2$ . The size of the effectively independent cells is  $2.0h^{-1} \text{ Mpc}$ . A simple Gaussian noise estimate counts all modes up to  $\Delta^2(k) < 0.2$ , which is perhaps surprisingly low.

For our noise estimates, we stacked simulations all at redshift  $z = 7$ . While the angular diameter distance does not change much to  $z \sim 20$ , the structure does evolve. We do not have access to the higher redshift outputs to test this effect, but one would expect a smaller non-linear scale to result in a smaller reconstruction noise.

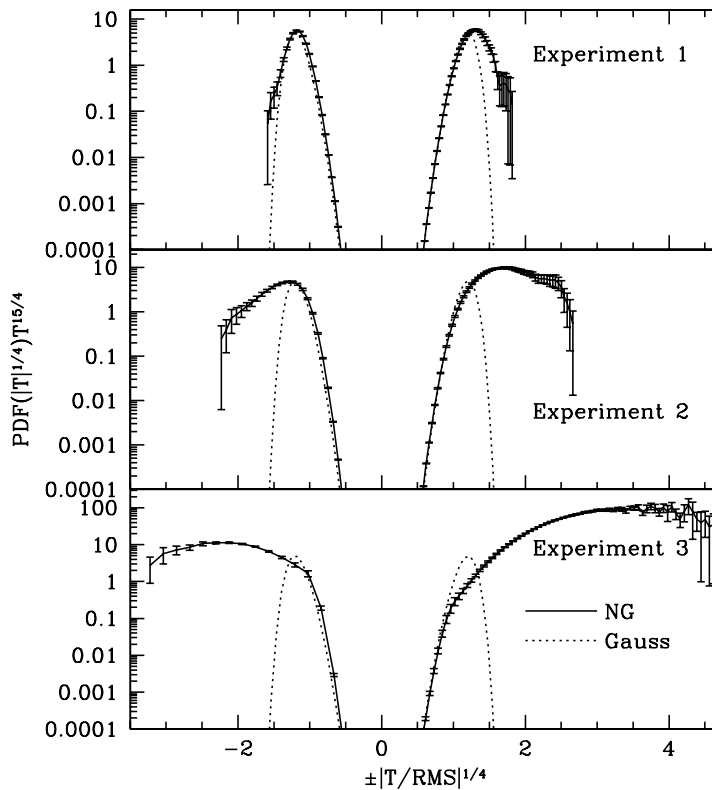


**Figure 6.** The PDF of maps smoothed with  $\kappa$  window are shown. The top, middle and bottom panel show the results with experimental noise cut offs 1, 2 and 3. The solid line is the PDF for maps smoothed with the  $\kappa$  window ( $T^\kappa$  in section 2.2.1). To see the full dynamic range on the x-axis, we plot the curve with  $\pm|T|^{1/4}$  as x-axis, and  $\text{PDF}(|T|^{1/4})|T|^{15/4}$  as the y-axis. The integral of the x-axis weighted by the y-axis will give  $\langle T^4 \rangle$ , which is basically a estimation of the reconstruction noise. The error bars are estimated from the 20 simulations. To compare with a Gaussian distribution, dotted lines are also plotted. The contributions to the  $\langle T^4 \rangle$  in experiment 1 mainly come from small fluctuation regions. In experiment 2, the large outliers play a more important role but one can still expect the curve to converge. In experiment 3, most contributions come from rare regions with high fluctuations. Caution should be exercised in the interpretation of the most non-linear scales, since a larger number of source samples may result in a different error. It is clear, however, that the noise has increased dramatically.

## 4.2 Future directions

A possible way to find the optimal window functions for non-Gaussian sources is to divide the window into  $N$  frequency bins  $W_1(\mathbf{k}_1, \mathbf{k}_2, \dots, \mathbf{k}_N)$ , and apply a numerical variation to those bins. The noise can be measured numerically by applying the estimator to the simulated sources. The process of searching for a optimal filter is equivalent to look for a minimum of reconstruction noise in  $N$  dimensional space  $\mathbf{k}_1, \mathbf{k}_2, \dots, \mathbf{k}_N$ . One could use a Newton–Raphson method to do this. In this paper we only considered the class of windows which are identical to the optimal Gaussian estimators with a hard cut off, as well as two weightings for shear and convergence.

One can also try to Gaussianize the sources by modifying the PDF of all the sources to be Gaussian. The physical explanation and details of Gaussianization can be found in Weinberg (1992). The basic idea is that every pixel should preserve its rank in the whole field during the Gaussianization process. During structure formation, the non-linear evolution at small scales should not destroy most of the information on the peaks and dips of the linear field. However, this Gaussianization process will change the power spectrum of sources, and the reconstructed lensing field will be biased. This is not a linear process, and the variation of power spectrum does not have analytical solution, and can only be measured numerically with simulated sources.

Recently it has been proposed that one could economically achieve brightness mapping of 21-cm emission at lower redshifts (Chang et al. 2007), potentially even with existing telescopes. If individual galaxies are not resolved, one can again ask the question of how one could reconstruct a lensing signal. This is very similar to the problem studied in this paper.

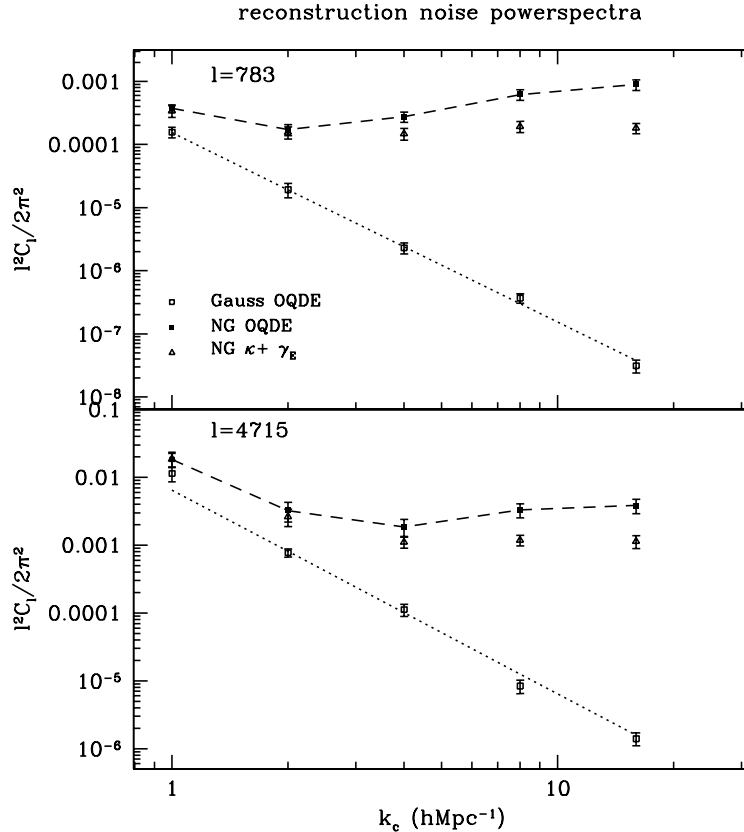


**Figure 7.** The reconstruction noise versus the cut off in the experimental noise. The top panel is for  $l_1 = 2\pi/L = 783$ , and the bottom panel is for  $l_2 = 6l_1 = 4715$ . The noise of Gaussian sources decreases as  $k_c$  increases, because of the increasing number of independent modes. The dotted lines are a least squares fitting power law  $N_0 k_c^{-3}$  to the Gaussian noises, and  $N_0 = 3.1 \times 10^{-2}, 1.3 \times 10^{-1}$  for top and bottom panels respectively. The dashed lines connect the non-Gaussian noise of the OQDE. The triangles are the reconstruction noise for the combined estimator, which is equal to the OQDE at larger scale  $k_c$  and about half an order of magnitude lower at large  $k_c$ . The noise of the non-Gaussian sources changes slowly and saturates or even increases at small scales.

## 5 CONCLUSION

In this paper, we developed the maximum likelihood estimator for the large-scale structure from the 21-cm emission of the neutral gas before the epoch of re-ionization. The convergence and shears can be constructed independently. To test the effects of non-Gaussianity, we applied our estimators to simulated data. The sources were generated by N-body simulations, because gas is expected to trace the total mass distribution. To investigate the influence of non-Gaussianity, we also use Gaussian sources which have the same power spectrum as the simulated sources. We applied our estimator and the OQDE on both the Gaussian and non-Gaussian sources. Though our estimators are derived in the simplified case of a constant convergence, the noise of our combined estimator of convergence and shear are the same as the OQDE for Gaussian sources. For a finite survey area, three extra constant modes can be recovered.

The non-Gaussian nature of the source can increase the error bar by orders of magnitude, depending on the experimental cut off scale. Shear construction is affected less by non-Gaussianity than the convergence field, and the combined estimator with non-Gaussian noise weights is a better choice than reconstructing with the OQDE. S/N can not be boosted infinitely by reducing the experimental noise, and achieves its maximum for a cut off around  $k_c^{\text{NG}} \approx 4h \text{ Mpc}^{-1}$ . Below that scale the S/N start to saturate or even decrease. The maximum S/N for non-Gaussian sources is equal to Gaussian sources with  $k_c^{\text{G}} \approx 2h \text{ Mpc}^{-1}$ , where the power spectrum of source is  $\Delta^2 \approx 0.2$  and the side length of the effectively independent cells is  $2.0h^{-1} \text{ Mpc}$ . The maximum S/N is greater than unity for  $l \lesssim 6000$ , which makes 21-cm lensing very competitive compared to optical approaches.

*Acknowledgments* We thank Oliver Zahn, Chris Hirata, Brice Ménard and Mike Kesden for helpful discussions. T.T. Lu thanks Pengjie Zhang, Zhiqi Huang, Hy Trac, and Hugh Merz for help in the early stage of the work.

## REFERENCES

- Barkana R., Loeb A., 2005, ApJ, 624, L65  
 Benton Metcalf R., White S. D. M., 2006, ArXiv Astrophysics e-prints  
 Chang T.-C., Pen U.-L., Peterson J. B., McDonald P., 2007, ArXiv e-prints, 709  
 Cooray A., 2004, New Astronomy, 9, 173  
 Efstathiou G., Bond J. R., White S. D. M., 1992, MNRAS, 258, 1P  
 Hilbert S., Benton Metcalf R., White S. D. M., 2007, ArXiv e-prints, 706  
 Hirata C. M., Seljak U., 2004, Phys. Rev. D, 70, 063526  
 Hoekstra H., Mellier Y., van Waerbeke L., Semboloni E., Fu L., Hudson M. J., Parker L. C., Tereno I., Benabed K., 2006, ApJ, 647, 116  
 Hu W., 2001a, Phys. Rev. D, 64, 083005  
 Hu W., 2001b, ApJ, 557, L79  
 Hu W., Okamoto T., 2002, ApJ, 574, 566  
 Hu W., White M., 2001, ApJ, 554, 67  
 Kaiser N., 1992, ApJ, 388, 272  
 Lewis A., Challinor A., 2006, Physics Reports, 429, 1  
 Limber D. N., 1954, ApJ, 119, 655  
 Mandel K. S., Zaldarriaga M., 2006, ApJ, 647, 719  
 Merz H., Pen U., Trac H., 2005, New Astronomy, 10, 393  
 Peacock J. A., Dodds S. J., 1996, MNRAS, 280, L19  
 Pen U., 2004, New Astronomy, 9, 417  
 Seljak U., Zaldarriaga M., 1996, ApJ, 469, 437+  
 Smith K. M., Zahn O., Doré O., 2007, Phys. Rev. D, 76, 043510  
 Smith R. E., Peacock J. A., Jenkins A., White S. D. M., Frenk C. S., Pearce F. R., Thomas P. A., Efstathiou G., Couchman H. M. P., 2003, MNRAS, 341, 1311  
 Spergel D. N. e. a., 2003, ApJS, 148, 175  
 Weinberg D. H., 1992, MNRAS, 254, 315  
 Zahn O., Zaldarriaga M., 2006, ApJ, 653, 922  
 Zaldarriaga M., Seljak U., 1999, Phys. Rev. D, 59, 123507

## APPENDIX A: NORMALIZATION AND NOISE OF THE ESTIMATOR

In the end of section 4, the numerical results of the noise of the estimators are shown. Here we will develop the analytical expression for

$$E_{\kappa}(\mathbf{k}_{\perp}) = b_{\kappa}(\mathbf{k}_{\perp})[\kappa(\mathbf{k}_{\perp}) + n(\mathbf{k}_{\perp})]. \quad (\text{A1})$$

For shear, a similar relationship holds even though  $b$  and  $n$  are not isotropic.

When  $\kappa$  is spatially variable,

$$\tilde{T}_b(\mathbf{x}) = T_b(\mathbf{x}_{\perp} - \mathbf{D}(\mathbf{x}_{\perp}), x_{\parallel}) = T_b(\mathbf{x}_{\perp}, x_{\parallel}) - \nabla_{\perp} T_b(\mathbf{x}_{\perp}, x_{\parallel}) \cdot \mathbf{D}(\mathbf{x}_{\perp}), \quad (\text{A2})$$

where  $\mathbf{D}(\mathbf{x}_{\perp}) = \mathbf{d}(\mathbf{x}_{\perp})\chi(z_s)$ , and  $\mathbf{d}(\mathbf{x}_{\perp})$  is the deflection angle. Therefore  $\kappa = \nabla_{\perp} \cdot \mathbf{D}$ .

Fourier transforming Eq. (27),

$$E_{\kappa}(\mathbf{k}_{\perp}) = \int d^2 x_{\perp} E_{\kappa}(\mathbf{x}_{\perp}) e^{-i\mathbf{k}_{\perp} \cdot \mathbf{x}_{\perp}} = \frac{1}{L} \int d^3 x \tilde{T}_{w_1}^{\kappa}(\mathbf{x}) \tilde{T}_{w_2}^{\kappa}(\mathbf{x}) e^{-i\mathbf{k}_{\perp} \cdot \mathbf{x}_{\perp}} - (2\pi)^2 \delta^{2D}(\mathbf{k}_{\perp}) V_{\kappa}. \quad (\text{A3})$$

$\tilde{T} = \tilde{T}_b + n$ , and noise is uncorrelated with the signal. The product in real space can be represented as a convolution in Fourier space

$$\int d^3 x e^{-i\mathbf{k}_{\perp} \cdot \mathbf{x}_{\perp}} \tilde{T}_{w_1}^{\kappa}(\mathbf{x}) \tilde{T}_{w_2}^{\kappa}(\mathbf{x}) = \int \frac{d^3 k'}{(2\pi)^3} \tilde{T}_{w_1}^{\kappa}(\mathbf{k}'_{\perp}, k'_{\parallel}) \tilde{T}_{w_2}^{\kappa}(\mathbf{k}_{\perp} - \mathbf{k}'_{\perp}, -k'_{\parallel}). \quad (\text{A4})$$

$$\tilde{T}_b(\mathbf{k}) = \int d^3 x e^{-i\mathbf{k} \cdot \mathbf{x}} T_b(\mathbf{x}_{\perp} - \mathbf{D}(\mathbf{x}_{\perp}), x_{\parallel}) = T_b(\mathbf{k}) - \int d^3 x e^{-i\mathbf{k} \cdot \mathbf{x}} \nabla_{\perp} T_b(\mathbf{x}_{\perp}, x_{\parallel}) \cdot \mathbf{D}(\mathbf{x}_{\perp}), \quad (\text{A5})$$

and the lensing introduced term can be further simplified as

$$\int d^3 x e^{-i\mathbf{k} \cdot \mathbf{x}} \nabla_{\perp} T_b(\mathbf{x}_{\perp}, x_{\parallel}) \cdot \mathbf{D}(\mathbf{x}_{\perp}) = \int d^3 x e^{-i\mathbf{k} \cdot \mathbf{x}} T_b(\mathbf{x}_{\perp}, x_{\parallel}) (i\mathbf{k}_{\perp} - \nabla_{\perp}) \cdot \mathbf{D}(\mathbf{x}_{\perp})$$

$$= \int \frac{d^2 k'_\perp}{(2\pi)^2} T_b(\mathbf{k}_\perp - \mathbf{k}'_\perp, k'_\parallel) (i\mathbf{k}_\perp - \nabla_\perp) \cdot \mathbf{D}(\mathbf{k}'_\perp). \quad (\text{A6})$$

The quadratic term in Eq. (A3) can be written as

$$\begin{aligned} \int d^3 x e^{-i\mathbf{k}_\perp \cdot \mathbf{x}_\perp} \tilde{T}_{w_1}^\kappa(\mathbf{x}_\perp, x_\parallel) \tilde{T}_{w_2}^\kappa(\mathbf{x}_\perp, x_\parallel) &= \int \frac{d^3 k'}{(2\pi)^3} W_1^\kappa(\mathbf{k}'_\perp, k'_\parallel) W_2^\kappa(\mathbf{k}_\perp - \mathbf{k}'_\perp, -k'_\parallel) [T_b(\mathbf{k}'_\perp, k'_\parallel) T_b(\mathbf{k}_\perp - \mathbf{k}'_\perp, -k'_\parallel) \\ &\quad - T_b(\mathbf{k}_\perp - \mathbf{k}'_\perp, -k'_\parallel)] \int \frac{d^2 k''_\perp}{(2\pi)^2} T_b(\mathbf{k}'_\perp - \mathbf{k}''_\perp, k'_\parallel) (i\mathbf{k}'_\perp - \nabla_\perp) \cdot \mathbf{D}(\mathbf{k}''_\perp) \\ &\quad - T_b(\mathbf{k}'_\perp, k'_\parallel) \int \frac{d^2 k'''_\perp}{(2\pi)^2} T_b(\mathbf{k}_\perp - \mathbf{k}'_\perp - \mathbf{k}'''_\perp, -k'_\parallel) (i(\mathbf{k}_\perp - \mathbf{k}'_\perp) - \nabla_\perp) \cdot \mathbf{D}(\mathbf{k}'''_\perp) \\ &\quad + \text{Noise}. \end{aligned} \quad (\text{A7})$$

Using the relationship that

$$\langle T_b(\mathbf{k}'_\perp, k'_\parallel) T_b(\mathbf{k}_\perp - \mathbf{k}'_\perp, -k'_\parallel) \rangle = (2\pi)^3 \delta^{3D}(\mathbf{k}_\perp, 0) P_{3D}(\mathbf{k}'_\perp, k'_\parallel), \quad (\text{A8})$$

we found that the expectation value of the first terms and the noise term in Eq. (A7) can cancel the last term in Eq. (A3). Note  $\delta(0) = \lim_{\Delta k \rightarrow 0} (\Delta k)^{-1} \sim (L/2\pi)$ , and  $W_2^\kappa(\mathbf{k}_\perp - \mathbf{k}'_\perp, -k'_\parallel) \sim W_2^\kappa(\mathbf{k}'_\perp, k'_\parallel)$  since  $\delta^{2D}(\mathbf{k}_\perp)$  is nonzero only when  $\mathbf{k}_\perp = 0$ . Similarly, the last two terms can be simplified. The normalization factor

$$b_\kappa(\mathbf{k}_\perp) = \frac{2}{k_\perp^2} \int \frac{d^3 k'}{(2\pi)^3} W_1^\kappa(\mathbf{k}'_\perp, k'_\parallel) W_2^\kappa(\mathbf{k}_\perp - \mathbf{k}'_\perp, -k'_\parallel) [(\mathbf{k}_\perp - \mathbf{k}'_\perp) \cdot \mathbf{k}_\perp P_{3D}(\mathbf{k}_\perp - \mathbf{k}'_\perp, -k'_\parallel) + \mathbf{k}'_\perp \cdot \mathbf{k}_\perp P_{3D}(\mathbf{k}'_\perp, k'_\parallel)]. \quad (\text{A9})$$

Similarly, replacing  $W_1^\kappa, W_2^\kappa$  by  $W_1^{\gamma_1}, W_2^{\gamma_1}$  ( $W_1^{\gamma_2}, W_2^{\gamma_2}$ ), and  $k_\perp^2$  by  $k_\perp^2 \cos 2\theta_{\mathbf{k}_\perp}$  ( $k_\perp^2 \sin 2\theta_{\mathbf{k}_\perp}$ ), we find the normalization factor for  $\gamma_1$  ( $\gamma_2$ ).

The noise of the estimator can be calculated in the absence of lensing:  $\langle |\hat{\kappa}(\mathbf{k}_\perp)|^2 \rangle = \langle \hat{\kappa}(\mathbf{k}_\perp) \hat{\kappa}^*(\mathbf{k}_\perp) \rangle$ . Since  $\langle |\hat{\kappa}(\mathbf{k}_\perp)|^2 \rangle = (2\pi)^2 \delta^{2D}(0) N_\kappa(\mathbf{k}_\perp)$  and  $\delta^{2D}(0) = \lim_{\Delta k \rightarrow 0} (\Delta k)^{-2} \sim (L/2\pi)^2$ , Wick's theorem gives

$$\begin{aligned} N_\kappa(\mathbf{k}_\perp) &= \frac{1}{b(\mathbf{k}_\perp)^2 L} \int \frac{d^2 k'_\perp}{(2\pi)^2} \int \frac{dk'_\parallel}{(2\pi)} \{ P_{3D}(\mathbf{k}_\perp - \mathbf{k}'_\perp, -k'_\parallel) P_{3D}(\mathbf{k}'_\perp, k'_\parallel) [W_1^\kappa(\mathbf{k}_\perp - \mathbf{k}'_\perp, -k'_\parallel) W_2^\kappa(\mathbf{k}'_\perp, k'_\parallel)]^2 \\ &\quad + P_{3D}(\mathbf{k}_\perp - \mathbf{k}'_\perp, -k'_\parallel) P_{3D}(\mathbf{k}'_\perp, k'_\parallel) \mathcal{F}^\kappa(\mathbf{k}_\perp - \mathbf{k}'_\perp, -k'_\parallel) \mathcal{F}^\kappa(\mathbf{k}'_\perp, k'_\parallel) \}. \end{aligned} \quad (\text{A10})$$

The first term is the convolution of  $P_{3D}(\mathbf{k}) W_1^\kappa(\mathbf{k})^2$  and  $P_{3D}(\mathbf{k}) W_2^\kappa(\mathbf{k})^2$ , and the second term is the convolution of  $P_{3D}(\mathbf{k}) \mathcal{F}^\kappa(\mathbf{k})$  with itself. The dimensionless quantity  $k_\perp^2 N_\kappa(\mathbf{k}_\perp) / (2\pi)$  is equivalent to  $l^2 C_l / (2\pi)$  in other literature.

This paper has been typeset from a  $\text{\TeX}/\text{\LaTeX}$  file prepared by the author.